Supplementary Information

Orbital Hanle magnetoresistance in a 3*d* transition metal

Giacomo Sala, Hanchen Wang, William Legrand, and Pietro Gambardella

Department of Materials, ETH Zurich, Hönggerbergring 64, 8093 Zurich, Switzerland
Email: giacomo.sala@mat.ethz.ch

S1 - Sample growth and characterization

Sample growth

All samples were grown by magnetron sputtering in a base pressure better than $1.5 \cdot 10^{-7}$ Torr. The $Si/SiO_2/Mn(t_{Mn})$ and $Si/SiO_2/Pt(5)$ samples were grown by DC sputtering in an Ar pressure of 3.7 mTorr and with a power of 5-10 W, which yielded a growth rate < 0.5 Å/s. Before the deposition of Mn and Pt, the Si/SiO_2 substrates were pre-sputtered for 90 s in a 15 mTorr Ar pressure with an RF power of 50 W. Mn and Pt were capped with $SiN_x(8)$ layers grown by RF sputtering to avoid natural oxidation in air.

The Mn and Pt layers of BiYIG/Mn(10) and BiYIG/Pt(5) were grown with a similar recipe. The BiYIG(15) garnet was grown from a stoichiometric target of $Bi_{0.8}Y_{2.2}Fe_5O_{12}$ by RF sputtering. First, the $Gd_3Ga_5O_{12}(111)$ (GGG) substrate was annealed for 1 h at 750 °C in a mixed Ar-O_2 atmosphere. BiYIG was subsequently grown with a power of 80 W in a mixed atmosphere and an Ar/O_2 flow rate of 100/6 sccm and total pressure of 3.8 mTorr. After annealing for 1 h, the sample was let cool down to room temperature, at which the Mn and Pt layers were grown as described above.

Crystalline structure

X-ray reflectrometry (XRR) and diffractometry (XRD) measurements were performed to verify the crystalline structure of the grown samples. In $Si/SiO_2/Mn(9)$ sample (Fig. S1a), the XRD signal is dominated by the peaks of the SiO_2 substrate. We identify only an additional faint feature at 135°, which could correspond to the (222) and/or (871) diffraction peak of γ-Mn and α-Mn, respectively. The small amplitude of this peak and the absence of other characteristic patterns indicate that Mn does not have a clear preferential crystal structure and is mostly polycrystalline or amorphous.

From the XRR measurements on BiYIG in Fig. S1b, we estimate a film thickness of 17 nm and a surface roughness of 0.74 nm. This result is in good agreement with the thickness estimate provided by the XRD measurement. As shown in Fig. S1c, the (444) peak of the GGG substrate at $\approx 51°$ is accompanied by the (444) peak of BiYIG at $\approx 50.5°$ and its Laue fringes. By fitting a Laue function to the XRD intensity [1, 2], we identify about 18-20 (111)-oriented planes, which correspond to a thickness of about 13-15 nm. The width of the central peak corresponds to an out-of-plane bulk unit cell of 1.2428 nm, which is consistent with that of $Bi_{0.8}Y_{2.2}Fe_5O_{12}$ [3, 4].

Magnetic properties

The magnetic properties of BiYIG were tested by means of ferromagnetic resonance measurements, which yielded an effective magnetization of 322 mT (330 mT), a damping of 0.0037 (0.0013), and an inhomogeneous linewidth of 0.7 mT (2.5 mT) in BiYIG/Mn (BiYIG/Pt).

Bulk Mn is nonmagnetic at least down to 90 K, where the transition to an antiferromagnetically-ordered state occurs [5, 6]. In fact, because antiferromagnetism is suppressed in disordered Mn films [6, 7], we do not expect an antiferromagnetic ground state in our samples. This is confirmed by measurements of the temperature-dependence of the magnetic moment in Fig. S2, where the curves are shown after subtraction of the magnetic contribution at 300 K. This contribution is overwhelmingly negative (diamagnetic) for all samples and originates from the SiO_2 substrate. Upon lowering the temperature, the magnetic moment of SiO_2 increases slightly, likely due to the presence of paramagnetic defects in SiO_2 [8, 9]. For the

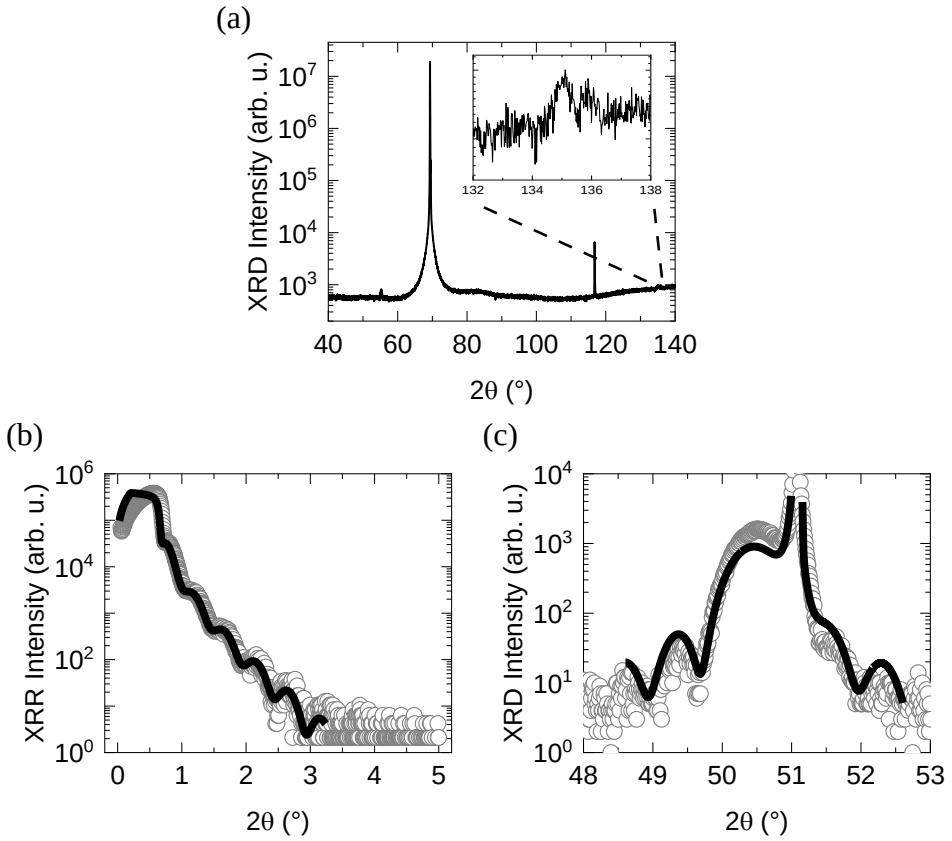

Figure S1. (a) XRD $\omega - 2\theta$ scans of SiO_2/Mn(10). (b) XRR 2θ scan of GGG/BiYIG. The solid line is the fit to the data [1]. (c) XRD ω-2θ scans of GGG/BiYIG. The solid line is a fit to the Laue function [1].

SiO_2/Pt and SiO_2/Mn samples, the increase of magnetic moment relative to 300 K is larger than for SiO_2 alone, reflecting the paramagnetic nature of the Pt and Mn films. However, the diamagnetic response of SiO_2/Mn does not differ appreciably from that of the substrate or SiO_2/Pt below 90 K, which corroborates the absence of any magnetic order in our Mn thin films. Increasing the external field only results in a larger diamagnetic contribution. This implies that, if there is any uncompensated magnetization in Mn, this must be smaller than about 2 kA/m, i.e., 0.002 μ_B/atom. These measurements and the observation that the HMR of Mn decreases with decreasing temperature prove that antiferromagnetism is not the origin of the large HMR of Mn.

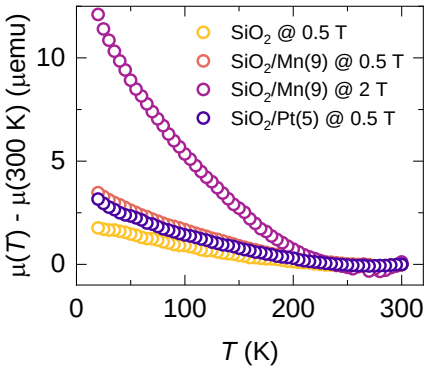

Figure S2. Magnetic moment of the Si/SiO_2, Si/SiO_2/Mn(9), and Si/SiO_2/Pt(5) samples as a function of temperature measured by SQUID magnetometry. The magnetic field was applied in the sample plane. The samples had dimensions of 5x5 mm^2.

S2 - Resistivity of Mn

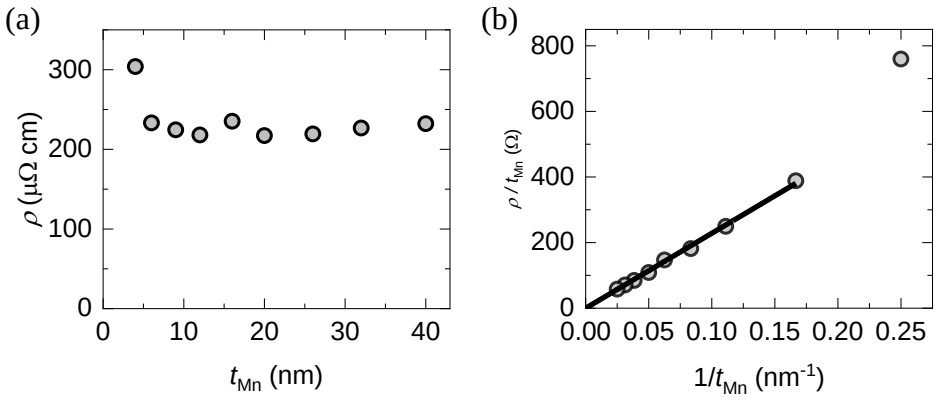

Figure S3. (a) Resistivity of Mn as a function of the film thickness. (b) Square resistance of Mn as a function of the inverse film thickness. The solid line is a linear fit with zero intercept.

The resistivity of Mn is independent of the film thickness t_{Mn} for $t_{\mathrm{Mn}} \geq 5$ nm (Fig. S3a). This trend is also corroborated by the constant slope of the square resistance $RW/L = \rho/t_{\mathrm{Mn}}$ with respect to t_{Mn} (W and L are the width and length of the Hall bar device used in the HMR measurements). This indicates that scattering of electrons off surfaces becomes relevant only in very thin films. In turn, this observation suggests that the typical distance between scattering centers (impurities, grain boundaries, defects) is < 5 nm. We speculate that such scattering centers may be the sources of the orbital relaxation because of the variation of the local crystal potential, and ultimately determine the orbital relaxation length.

S3 - Quantitative analysis of the Hanle magnetoresistance

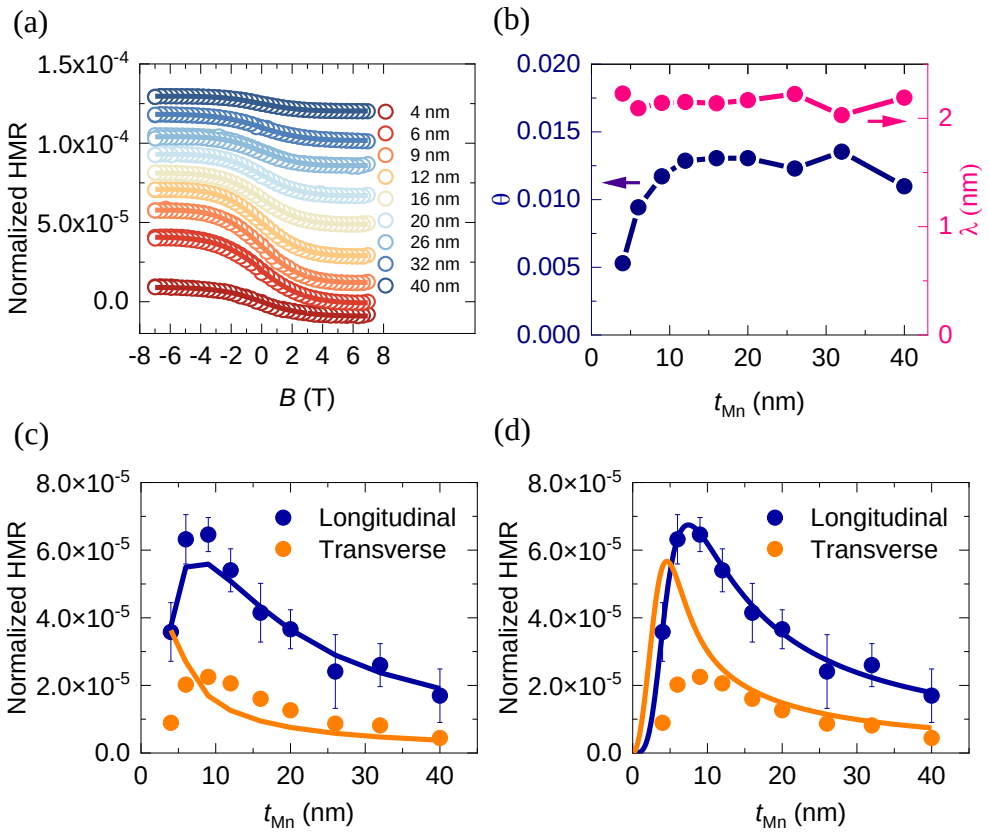

Figure S4. (a) Normalized transverse HMR as a function of the out-of-plane magnetic field in Mn films with different thickness. The solid lines are fits to Eq. 4 in the main text. (b) Thickness dependence of the orbital Hall angle and diffusion length obtained from the fits in (a). (c) Best simultaneous fit of the longitudinal and transverse HMR with shared parameters. (d) Thickness dependence of the longitudinal and transverse HMR predicted by Eqs. 3-4 on the basis of the parameters in the third row of Table I.

The quantitative analysis of the Hanle effect with the aid of Eqs. 3-4 is not trivial, and requires caution because of the interdependence of the unknown parameters (θ, λ, D). This implies that different sets of parameters could yield equally good fits. In Ref. [10], this difficulty was overcome by fixing the spin Hall angle (θ) and the spin diffusion length (λ) of Pt, which leaves the diffusion coefficient (D) as the unique free parameter. This approach is not possible for Mn because all three quantities (θ, λ, D) are unknown. Although spin pumping and spin-orbit torque measurements could provide an estimate of θ and λ [11, 12], the discrepancy between the reported values (which is possibly related to the spin vs orbital origin of the measured signals) does not allow for fixing any parameter. We therefore resorted to a different strategy. First, we performed a global fit of Eq. 4 to all the transverse HMR curves of Mn, i.e., all thicknesses, with partially-shared parameters (Fig. S4a). In particular, the diffusion coefficient was set to be common to all datasets, whereas the orbital Hall angle and the diffusion length were let to vary with the Mn thickness. This choice is justified by the independence of the electrical resistivity of the film thickness (Fig. S3), which, to first order, translates into a constant diffusion coefficient. As shown in Fig.

S4a, this approach yields a good fit of all the datasets. Interestingly, we find that the orbital Hall angle increases with the Mn thickness up to $t_{Mn} = 12$ nm, whereas the diffusion length remains constant with t_{Mn}. The values of θ and λ reported in Table 1 relative to the transverse HMR are the average of the data in Fig. S4b.

Armed with these results, we could then fit all the other datasets (field dependence of the longitudinal resistance, thickness dependence of the longitudinal and transverse resistance) by using the parameters estimated from the fits in Fig. S4a as starting point of the fitting routine. As reported in Table 1, this approach yields reasonably consistent estimates of the orbital Hall angle, diffusion length, and diffusion time. We note, however, that there is a discrepancy between the predicted and measured thickness dependence of the longitudinal and transverse HMR (see Fig. S4c,d). Equations 3-4 in the main text predict that the longitudinal and transverse HMR reach their maximum at different thicknesses. For example, if we consider the parameters extracted from the thickness dependence of the longitudinal HMR (third row in Table 1), we expect the transverse HMR to peak at about 5 nm (Fig. S4d). In contrast, the measured transverse HMR is maximum at about 10 nm, similar to the longitudinal HMR. A previous study of the HMR of Pt also found that the longitudinal and transverse HMR peak at the same thickness [13]. Because of this discrepancy between the expected and observed thickness dependence, we were not able to fit simultaneously, i.e, with shared parameters, and in a satisfactory manner the thickness dependence of the longitudinal and transverse HMR (Fig. S4c). The origin of this issue remains unclear.

Table I: Transport parameters of Mn and Pt thin films obtained from HMR measurements of the longitudinal (R) and transverse (R_H) resistance: resistivity (ρ), spin-orbital Hall angle (θ), diffusion length (λ), relaxation time (τ). The source indicates the datasets from which these parameters were obtained: the field dependence of the longitudinal and transverse resistance [$R(B), R_H(B)$], and the thickness dependence of the longitudinal and transverse HMR [HMR(t_{Mn}), HMR$_H$(t_{Mn})]. The asterisk (*) denotes the parameters that were fixed in the fitting routine.

Sample	ρ [$\mu\Omega$ cm]	θ	λ [nm]	τ [ps]	Source
SiO_2/Mn(9)	225	0.016	2.1*	1.5	$R(B)$
	225	0.011	2.1	1.6	$R_H(B)$
SiO_2/Mn(t_{Mn})	230	0.013	3.3	4.2	HMR(t_{Mn})
	230	0.011	3.3	0.9	HMR$_H$(t_{Mn})
BiYIG/Mn(10)		0.015	2.0*	1.8	$R(B)$
		0.008	2.0*	1.7	$R_H(B)$
SiO_2/Pt(5)	58	0.033	2.0*	0.8	$R(B)$
	58	0.019	2.0*	0.9	$R_H(B)$
BiYIG/Pt(5)		0.035	2.0*	0.7	$R(B)$
		0.029	2.0*	0.5	$R_H(B)$
Pyrex/Pt(7)[a]	90	0.056*	0.9*	0.1	$R(B)$
Pyrex/Pt(3)[a]	106	0.056*	0.8*	0.2	$R(B)$
YIG/Pt(7)[a]	63	0.056*	1.3*	0.3	$R(B)$
Al_2O_3/Pt(5.2)[b]	<50	0.029	1.7	2.9	$R_H(B)$

[a] Ref. [10]
[b] Ref. [13]

S4 - Hanle magnetoresistance in BiYIG/Mn and BiYIG/Pt

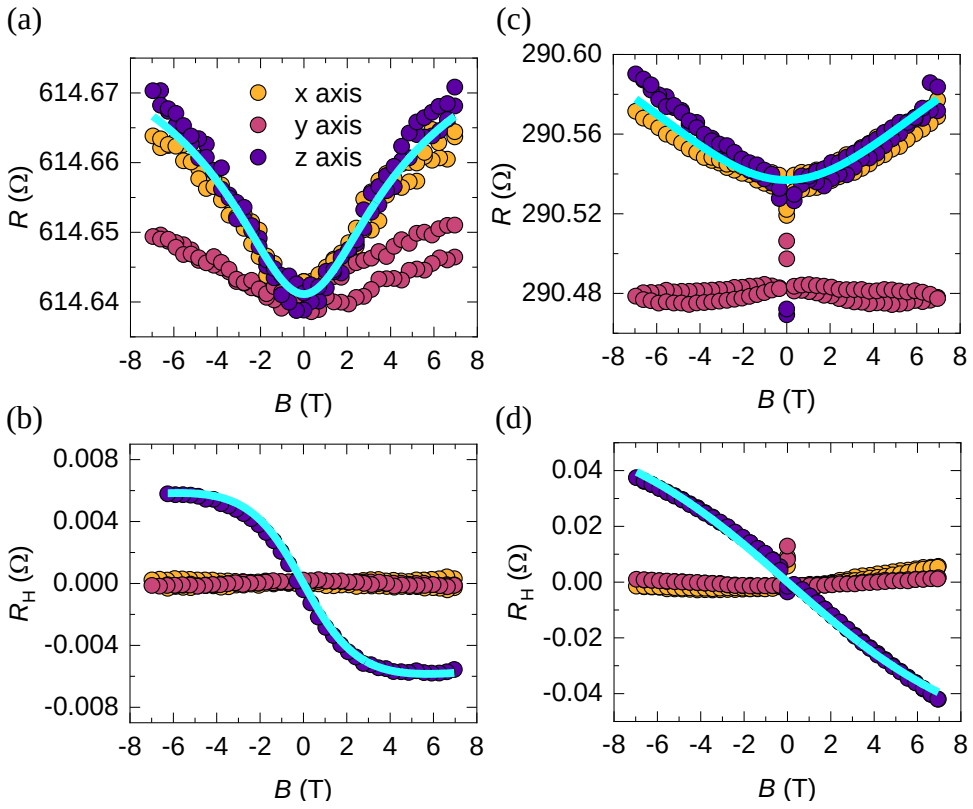

Figure S5. (a-b) Longitudinal and transverse resistance of BiYIG/Mn(10) as a function of the magnetic field applied along the three axes. The solid lines are fits to Eqs. 3-4. The ordinary Hall effect was subtracted from the transverse resistance. (c-d) Same as (a-b) for BiYIG/Pt(5). The fit of Eq. 4 to the transverse resistance is not perfect because of the impossibility of subtracting the ordinary Hall effect.

The HMR and SMR measurements in BiYIG/Mn and BiYIG/Pt were performed on 4×4 mm^2 unpatterned samples because the Ar ion etching was found to degrade the properties of the BiYIG-nonmagnet interface. The electrical contacts (wire bonds) necessary to measure the transverse and longitudinal resistance were placed at the sample corners. Figure S5 shows the HMR measured in BiYIG/Mn(10) and BiYIG/Pt(5), which is similar to that of the corresponding single layers grown on Si/SiO_2. The longitudinal resistance increases with the magnetic field applied along the directions (x and z) orthogonal to the spin or orbital polarization (y). When the field is applied along y, the resistance is approximately constant (Pt) or increases slightly (Mn), possibly because of a finite ordinary magnetoresistance. Note that we did not find evidence of the ordinary magnetoresistance in other Mn films. Interestingly, the resistance of Pt shows an abrupt jump in the vicinity of zero that is not observed in Mn. This jump is determined by the SMR of the BiYIG/Pt bilayers. When the field along x or z reaches ≈ 0.5 T, the magnetization of BiYIG is saturated in a direction orthogonal to the spin polarization, which results in the maximum SMR. Further increase of the field leads to the appearance of the HMR. In contrast, when the magnetization of BiYIG is saturated along y, the SMR is minimum and the HMR is also zero. The absence of jumps in

the vicinity of zero field in the BiYIG/Mn sample provides further evidence of the very small SMR of this bilayer. Finally, the Hanle effect manifests itself also in the transverse resistance when the field is oriented out of the plane. Both the longitudinal and transverse HMR can be analyzed with the aid of Eqs. 3-4. The parameters extracted from the fit are reported in Table 1, and are in good agreement with those relative to the Mn and Pt single layers.

[1] A. M. Miller, M. Lemon, M. A. Choffel, S. R. Rich, F. Harvel, and D. C. Johnson, Extracting information from X-ray diffraction patterns containing Laue oscillations, Zeitschrift für Naturforschung B **77**, 313 (2022).

[2] C. Du, H. Wang, P. C. Hammel, and F. Yang, Y3Fe5O12 spin pumping for quantitative understanding of pure spin transport and spin Hall effect in a broad range of materials (invited), Journal of Applied Physics **117**, 172603 (2015), arXiv:1410.1597.

[3] S. Kahl and A. M. Grishin, Enhanced Faraday rotation in all-garnet magneto-optical photonic crystal, Applied Physics Letters **84**, 1438 (2004).

[4] L. Caretta, S.-H. Oh, T. Fakhrul, D.-K. Lee, B. H. Lee, S. K. Kim, C. A. Ross, K.-J. Lee, and G. S. D. Beach, Relativistic kinematics of a magnetic soliton, Science **370**, 1438 (2020).

[5] S. Murayama and H. Nagasawa, Magnetoresistance in Antiferromagnetic α-Mn Metal, Journal of the Physical Society of Japan **43**, 1216 (1977).

[6] F. Boakye and K. G. Adanu, The Neel temperature of a-Mn thin films, Thin Solid Films **279**, 29 (1996).

[7] F. Boakye and A. D. Grassie, The influence of deposition parameters on the low temperature resistivity of α-Mn thin films, Thin Solid Films **221**, 224 (1992).

[8] E. H. Poindexter and W. L. Warren, Paramagnetic Point Defects in Amorphous Thin Films of SiO2 and Si3 N 4: Updates and Additions, Journal of The Electrochemical Society **142**, 2508 (1995).

[9] L. Skuja, M. Hirano, H. Hosono, and K. Kajihara, Defects in oxide glasses, physica status solidi (c) **2**, 15 (2005).

[10] S. Vélez, V. N. Golovach, A. Bedoya-Pinto, M. Isasa, E. Sagasta, M. Abadia, C. Rogero, L. E. Hueso, F. S. Bergeret, and F. Casanova, Hanle Magnetoresistance in Thin Metal Films with Strong Spin-Orbit Coupling, Physical Review Letters **116**, 016603 (2016), arXiv:1502.04624.

[11] C. Du, H. Wang, F. Yang, and P. C. Hammel, Systematic variation of spin-orbit coupling with d-orbital filling: Large inverse spin Hall effect in 3d transition metals, Physical Review B **90**, 140407 (2014), arXiv:1410.1590.

[12] G. Sala and P. Gambardella, Giant orbital Hall effect and orbital-to-spin conversion in 3d, 5d, and 4f metallic heterostructures, Physical Review Research **4**, 033037 (2022).

[13] J. Li, A. H. Comstock, D. Sun, and X. Xu, Comprehensive demonstration of spin Hall Hanle effects in epitaxial Pt thin films, Physical Review B **106**, 184420 (2022).